2-8-2019

Ferroelectric polarization control of magnetic anisotropy in PbZr0.2Ti0.8O3/La0.8Sr0.2MnO3 heterostructures

Anil Rajapitamahuni
University of Nebraska - Lincoln

L. L. Tao
University of Nebraska-Lincoln, ltao2@unl.edu

Y. Hao
University of Nebraska - Lincoln

Jingfeng Song
University of Nebraska - Lincoln

Xiaoshan Xu
University of Nebraska - Lincoln

See next page for additional authors

Rapid Communications

Ferroelectric polarization control of magnetic anisotropy in $PbZr_{0.2}Ti_{0.8}O_3/La_{0.8}Sr_{0.2}MnO_3$ heterostructures

A. Rajapitamahuni, L. L. Tao, Y. Hao, J. Song, X. Xu, E. Y. Tsymbal, and X. Hong*
Department of Physics and Astronomy & Nebraska Center for Materials and Nanoscience, University of Nebraska−Lincoln, Lincoln, Nebraska 68588-0299, USA

(Received 27 March 2018; revised manuscript received 30 December 2018; published 8 February 2019)

The interfacial coupling between the switchable polarization and neighboring magnetic order makes ferroelectric/ferromagnetic composite structures a versatile platform to realize voltage control of magnetic anisotropy. We report the nonvolatile ferroelectric field effect modulation of the magnetocrystalline anisotropy (MCA) in epitaxial $PbZr_{0.2}Ti_{0.8}O_3$ (PZT)/$La_{0.8}Sr_{0.2}MnO_3$ (LSMO) heterostructures grown on (001) $SrTiO_3$ substrates. Planar Hall effect measurements show that the in-plane magnetic anisotropy energy in LSMO is enhanced by about 22% in the hole accumulation state compared to the depletion state, in quantitative agreement with our first-principles density functional theory calculations. Modeling the spin-orbit coupling effect with second-order perturbation theory points to the critical role of the *d*-orbital occupancy in controlling MCA. Our work provides insights into the effect of ferroelectric polarization on the magnetic anisotropy at the composite multiferroic interfaces, paving the path for their implementation into high-performance, low-power spintronic applications.

DOI: 10.1103/PhysRevMaterials.3.021401

Multiferroic heterostructures consisting of ferroelectric and ferromagnetic layers have garnered significant research interest over the last decade as a model system for examining the interfacial magnetoelectric (ME) coupling [1–4]. Compared to single-phase multiferroics, where the intrinsic ME coupling coefficients are often weak, the composite heterostructures can be engineered to achieve orders-of-magnitude enhancement in the coupling strength [2], making them a viable material platform for developing high-performance, low-power spintronic devices, such as voltage-controlled magnetic memories and spin field effect transistors (FETs) [4–6]. The nonvolatile, bistable polarization and large bound charge density intrinsic to ferroelectrics also present them distinct advantages over the conventional dielectrics in building the composite ME devices.

For spintronic applications, it is of particular interest to realize voltage control of magnetic anisotropy [7], a critical parameter for engineering the spin switching dynamics and optimizing the data retention [8–10]. It has been theoretically predicated that ferroelectric polarization reversal can induce sizable changes in the magnetocrystalline anisotropy (MCA) in a neighboring magnetic material [11–13]. The epitaxial heterostructure based on the perovskite ferroelectric (or multiferroic) oxide and strongly correlated manganite is a promising material candidate for achieving such control, leveraging the highly tunable magnetic states in manganites via charge and/or strain modulation and the large interfacial ME coupling coefficient [14–23]. Compared to the strain-induced modulation of MCA [24], the polarization effect is mediated by charge without altering the strain state in the system, thus minimizing the mechanical stress in the composite multiferroic for operation in the two nonvolatile states. In previous studies, ferroelectric field effect tuning of magnetic-anisotropy-associated magnetotransport properties, such as the anisotropic magnetoresistance (AMR), has been reported in epitaxial (Pb, Zr)TiO_3 (PZT)/$La_{1-x}Sr_xMnO_3$ (LSMO) heterostructures [15,22]. However, due to the high carrier density in the correlated oxides, pronounced modulation can only be achieved in ultrathin channels [4], and it is highly challenging to map out the magnetic energy landscape in samples with such limited volumes. To date, direct realization of ferroelectric-polarization-controlled magnetic anisotropy has not been experimentally demonstrated and a microscopic understanding of the interfacial coupling mechanism is yet to be gained.

In this work, we report the nonvolatile ferroelectric field effect modulation of the in-plane MCA in an ultrathin $La_{0.8}Sr_{0.2}MnO_3$ film via switching the polarization of an interfacial $PbZr_{0.2}Ti_{0.8}O_3$ layer. Planar Hall effect (PHE) measurements reveal biaxial magnetic anisotropy in LSMO, with the magnetic anisotropy energy (MAE) in the hole accumulation state about 22% higher than in the depletion state. Comparing the results to those obtained in single-layer $La_{1-x}Sr_xMnO_3$ films with different chemical compositions reveals the charge-mediated nature of the coupling. Our theoretical modeling based on first-principles density functional theory (DFT) combined with second-order perturbation to spin-orbit coupling (SOC) indicates the critical role of *d*-orbital occupancy in the doping dependence of MCA. As LSMO is widely utilized as the spin injection layer for novel multiferroic tunnel junctions [5,6], our results provide critical insights into engineering the performance of these composite multiferroic structures for spintronic applications.

We deposited *in situ* epitaxial PZT/LSMO heterostructures on (001) $SrTiO_3$ (STO) substrates using off-axis radio-frequency magnetron sputtering (see Supplemental Material [25] for growth and characterization details). Figure 1(a)

*xia.hong@unl.edu

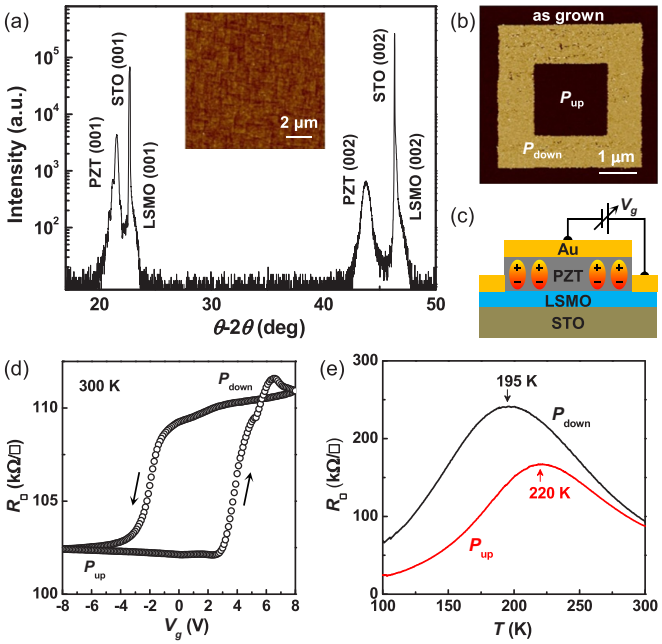

FIG. 1. (a) X-ray θ–2θ scan of a 250 nm PZT/4 nm LSMO on STO. Inset: AFM topography of the sample. (b) PFM phase image of a domain structure written with -6 V (P_{up}) and $+6$ V (P_{down}) bias voltage applied to a scanning AFM tip. (c) Device schematic. (d) $R_{\square}(V_g)$ hysteresis taken at 300 K. (e) $R_{\square}(T)$ for both polarization states, with the corresponding T_p marked with the arrows.

shows the x-ray θ–2θ scan of a 250 nm PZT/4 nm LSMO heterostructure, which reveals high crystallinity with no appreciable impurity phase. These samples possess smooth surface morphology with a typical root-mean-square surface roughness of $\sim$5 Å [Fig. 1(a) inset]. In the as-grown state, the PZT layer is uniformly polarized in the up orientation (P_{up}), as characterized by the piezoresponse force microscopy (PFM) measurements [Fig. 1(b)]. The heterostructure was fabricated into FET devices [Fig. 1(c)] using optical lithography followed by Au deposition, where the LSMO channel was patterned into the Hall-bar configuration. The current channel is along the [100] direction, using the pseudocubic notation, with the channel length/width of 10–40 μm and the aspect ratio of 1 or 2. The magnetotransport measurements were performed using a Quantum Design Physical Property Measurement System combined with Keithley 2400 SourceMeters.

Figure 1(d) shows the room-temperature sheet resistance ($R_{\square}$) of LSMO as a function of gate voltage V_g across the PZT layer taken on a FET device. LSMO exhibits a well-defined resistance hysteresis that follows the ferroelectric polarization switching. The P_{up} (P_{down}) state corresponds to hole accumulation (depletion), leading to lower (higher) channel resistance [14]. The resistance switching occurs at about -2.0 V and $+3.8$ V for the P_{up} and P_{down} states, respectively. The lower coercive voltage suggests that the P_{up} state is energetically more favorable, in agreement with the as-grown polarization. Such polarization asymmetry has been widely observed in epitaxial ferroelectric thin films and can be attributed to the asymmetric screening electrodes [26,27].

We then characterized the effect of ferroelectric polarization on the temperature dependence of resistance in LSMO. Figure 1(e) shows $R_{\square}(T)$ of a device after the PZT gate was polarized to the P_{up} (P_{down}) state by a -6 V ($+6$ V) voltage pulse. At this composition ($x = 0.2$), LSMO exhibits semiconducting behavior at high temperature, followed by metallic behavior at low temperature. The change of metallicity can be correlated with the magnetic transition from paramagnetic to ferromagnetic state upon cooling [28], even though the resistance peak temperature T_p may not precisely match the Curie temperature T_C in ultrathin LSMO films, likely due to the different length scales of the electrical and magnetic dead layers [29,30]. The T_p is about 220 K for the accumulation state (P_{up}) and 195 K for the depletion state (P_{down}), similar to previous reports on PZT/LSMO heterostructures with the same composition [16,17] and comparable to that of the single-layer 4 nm LSMO films (Supplemental Material [25]). The 25 K shift of T_p is a strong indication of the modulation of the magnetic state in the sample.

Previous studies of the interfacial ME coupling in PZT/LSMO heterostructures have focused on the modulation of the global magnetic order, such as T_C and magnetization [14,16,17]. Quantitative assessment of the change in magnetic anisotropy requires probing the angular dependence of magnetic energy, which is challenging for conventional magnetometry techniques due to the limited volume of the interfacial LSMO layer that can be tuned by the field effect. The PHE technique, on the other hand, directly probes the magnetization direction while being insensitive to the magnetoresistance background, presenting a powerful tool to quantify the magnetic anisotropy in LSMO thin films and nanostructures [31,32]. In the ferromagnetic state, LSMO exhibits sinusoidal dependences of the longitudinal (R_{xx}) and transverse (R_{xy}) resistance on the angle φ between current and in-plane magnetization [Fig. 2(a)]:

$$R_{xx} = R_{\perp} + (R_{\parallel} - R_{\perp})\cos\varphi^2,$$
$$R_{xy} = (R_{\parallel} - R_{\perp})\sin\varphi\cos\varphi, \quad (1)$$

known as the AMR and PHE, respectively [33,34]. Here, $R_{\parallel}(R_{\perp})$ is the resistance value measured with current parallel (perpendicular) to the magnetization. To investigate the effect of magnetic field H on the AMR and PHE, we first applied an in-plane H of 6 k Oe to set LSMO in a single magnetic domain state, and then measured R_{xx} and R_{xy} as functions of the angle θ between the field H and current I at different magnetic fields [Fig. 2(b)]. The measurements were performed at 125 K to achieve optimal signal-to-noise ratio for the planar Hall resistance (see Supplemental Material [25]). At a high magnetic field, where the Zeeman energy exceeds the MAE, magnetization follows the magnetic field direction, i.e., $\theta \approx \varphi$. This is the case at $H = 1000$ Oe, as shown in Fig. 2(b). Both the AMR (R_{AMR}) and PHE (R_{PHE}) resistances, defined as the oscillatory terms in R_{xx} and R_{xy}, respectively, exhibit sinusoidal θ dependence that can be well depicted by Eq. (1). The amplitudes of R_{AMR} and R_{PHE} are higher in the depletion state, with the ratio between the two states to be about 3.5 ± 0.2.

At a lower magnetic field, the MAE starts to dominate the Zeeman energy and the magnetization prefers to be aligned

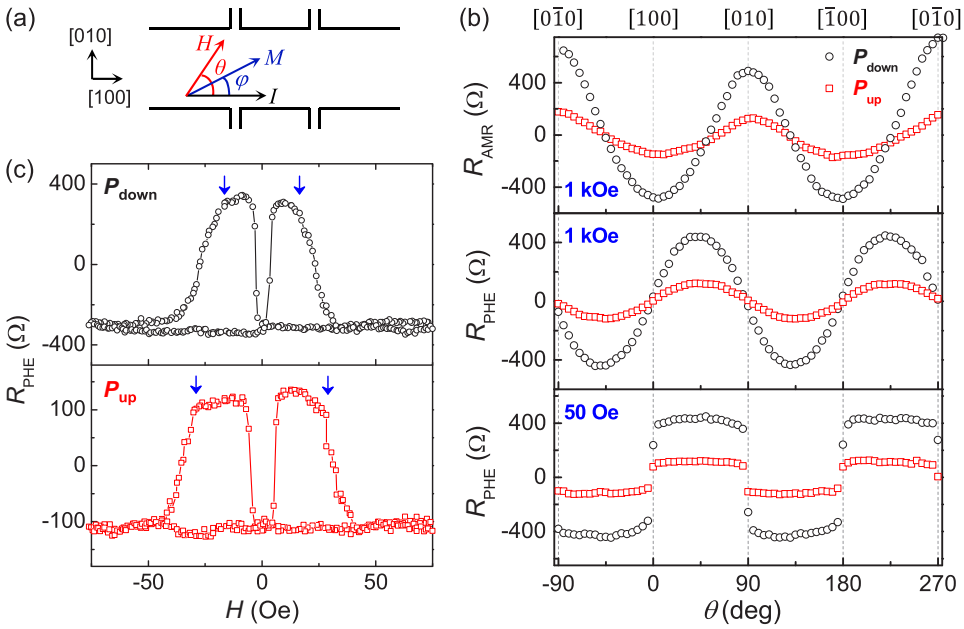

FIG. 2. AMR and PHE taken on a PZT/4 nm LSMO heterostructure. (a) Schematic of the measurement setup. (b) θ dependence of R_{AMR} at 1 kOe (upper panel), R_{PHE} at 1 kOe (middle panel), and 50 Oe (lower panel) at 125 K for both polarization states of PZT. (c) $R_{\mathrm{PHE}}(H)$ at 125 K for both polarization states. The arrows serve as a guide to the eye.

with the easy axis rather than following the magnetic field direction, i.e., $\theta \neq \varphi$. When strained on (001) STO substrates, LSMO thin films exhibit biaxial in-plane MCA, with the easy axes along the ⟨110⟩ directions [34,35]. At 50 Oe, R_{PHE} reveals abrupt resistance jumps between two distinct resistance levels at $\theta = \pm n\pi/2$, with each level reflecting the magnetization pinning to one of the two easy axes, i.e., [1$\bar{1}$0] and [110]. This effect is also clearly manifested in the switching hysteresis in R_{PHE} while sweeping H along the direction close to the [010] axis ($\theta \approx 95°$) [Fig. 2(c)]. As the applied field changes sign, the magnetization reversal is accomplished via two 90° rotations. Each rotation flips the magnetization to a different pinning axis, leading to a sharp change in the R_{PHE} level. The switching hysteresis closely resembles that of magnetic/multiferroic tunnel junctions [5] without involving a multilayer structure. Besides manganites [34,36], such magnetic-field-controlled bistable signals have been realized in the AMR and PHE resistances in a wide range of magnetic materials, including the ferromagnetic semiconductors [37], magnetite [38], and noncollinear magnetic oxide superlattices [39], and can be utilized to represent the binary logic in magnetic data-storage applications [39,40].

Comparing the switching hystereses for the two polarization states [Fig. 2(c)], we note that the resistance switching in the P_{up} state occurs at much higher magnetic fields, signaling a change in the magnetic energy in LSMO. This change can be quantified by identifying the anisotropy field H_1 in both polarization states, defined as the critical field over which the magnetization follows the magnetic field in coherent rotation [41]. To evaluate the angular relation between the magnetization and magnetic field, we normalized the θ dependence of R_{PHE} at different magnetic fields, and extracted the angle φ between the magnetization and current using $\varphi = \frac{1}{2}\sin^{-1}(R_{\mathrm{PHE}}/R_{\mathrm{PHE,max}})$ [Eq. (1)]. The relation between φ and θ is a direct manifestation of the energy competition between the Zeeman energy and anisotropy energy, and can be used to quantify the MCA [31]. Compared to previous studies exploiting the AMR to evaluate the magnetic anisotropy [15,22], the PHE has distinct advantages as it is not susceptible to complicating factors associated with spin scattering [33] and the pronounced magnetoresistance background. Figure 3(a) shows $\varphi(\theta)$ extracted from $R_{\mathrm{PHE}}(\theta)$ within the $\theta = [-45°, 45°]$ quadrant at different magnetic fields for the P_{up} and P_{down} states, where φ exhibits strong pinning to the [1$\bar{1}$0] and [110] directions ($\varphi = \pm 45°$) at low fields. With increasing magnetic field, the nonlinearity of $\varphi(\theta)$ gradually diminishes, while at 1000 Oe, a linear relation is recovered for both polarization states. To quantify the nonlinearity, we calculated the residual sum of squares (RSS) of the linear fit to $\varphi(\theta)$: $\mathrm{RSS} = \Sigma_i[\varphi(\theta_i) - \theta_i]^2$. As shown in Fig. 3(b), RSS first

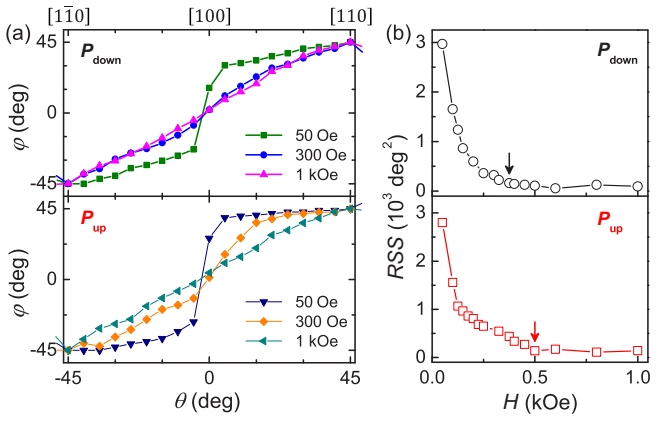

FIG. 3. (a) Extracted φ vs θ at different magnetic fields and (b) *RSS* vs H for the PZT/4 nm LSMO heterostructure in both polarization states of PZT. The arrows mark the corresponding anisotropy fields.

decreases with increasing H until the value saturates beyond the anisotropy field, at which we considered as the $\varphi \approx \theta$ condition was reached. We thus identified the anisotropy fields to be about 400 ± 12 Oe for the P_{down} state and 500 ± 25 Oe for the P_{up} state.

From the coherent rotation model [35,41], the anisotropy field H_1 is related to the biaxial magnetic anisotropy constant K_1 as $H_1 = 2K_1/M$, where M is the magnetization. For bulk $La_{1-x}Sr_xMnO_3$, the saturation magnetization is $4-x\,\mu_B$/Mn, and x corresponds to the hole concentration [28]. As the polarization field modulates the carrier density in LSMO, it also changes the magnetization. Previous studies of PZT/LSMO heterostructures of the same composition have shown that the polarization reversal leads to a change of the Mn valence state by about 0.1 hole/Mn [17]. Assuming that the P_{up} and P_{down} states induce the same amount of doping change in LSMO, i.e., 0.05 hole/Mn, we expect the low-temperature magnetization of the LSMO layer to be about $3.85\,\mu_B$/Mn ($3.75\,\mu_B$/Mn) for the depletion (accumulation) state. Superconducting quantum interference device (SQUID) measurements taken on single-layer LSMO show that the magnetization at 125 K is about 79% of the 10 K value (see Supplemental Material [25]). Using this ratio, we estimated the magnetization value at 125 K to be $3.04\,\mu_B$/Mn in depletion and $2.96\,\mu_B$/Mn in accumulation. Based on the H_1 and magnetization values, we deduced the biaxial MAE density E_{MAE} to be $9.7(3) \times 10^4$ erg/cm^3 in the depletion state, which increases by about 22% to $1.18(6) \times 10^5$ erg/cm^3 in the accumulation state. Note that we assumed the polarization control of magnetization can extend to the entire LSMO thickness (about 2.5 nm) above the magnetic dead layer, which is reasonable considering the reported magnetic modulation lengths at ferroelectric/LSMO interfaces [19,23]. The enhanced MAE with increasing hole doping is consistent with previous results obtained using ionic liquid gating [42].

To gain a microscopic understanding of the experimental observations, we performed first-principles DFT calculations of the MAE in LSMO with various doping levels using the plane-wave ultrasoft pseudopotential [43] method implemented in the Quantum ESPRESSO program [44], with the exchange-correlation functional treated using the generalized gradient approximation (GGA) [45]. To mimic the experimental condition for the ferroelectric polarization doping, we exploited the atomic structure of bulk $La_{0.8}Sr_{0.2}MnO_3$ in the calculations, with the in-plane lattice constant strained to the theoretical value of STO and the out-of-plane lattice constant and other atomic coordinates fully relaxed. The details of the modeling can be found in the Supplemental Material [25] and Refs. [46,47]. The total energies were calculated self-consistently for magnetization pointing along different in-plane orientations, which reveals a uniaxial anisotropy with the easy axis along the orthorhombic $\langle 100\rangle_o$ directions, corresponding to one of the pseudocubic $\langle 110\rangle$ axes. The experimentally observed biaxial anisotropy likely results from the presence of crystal twinning to conform to the cubic symmetry of the STO substrate [31,48]. The MAE was calculated as the total energy difference between the orthorhombic $\langle 100\rangle_o$ and $\langle 110\rangle_o$ directions for doping levels in the range $x = 0.15$–0.3. Given that the presence of crystal twinning would affect the magnitude of the energy density extracted from a global transport measurement, we have focused on the relative change of MAE, assuming the twinning structure is unchanged during the polarization reversal (see Supplemental Material [25]). Figure 4(a) shows the calculated MAE normalized to the value at $x = 0.2$ as a function of the doping level. The MAE increases almost linearly with increasing x, with $E_{\text{MAE}}/E_{\text{MAE}}(x = 0.2)$ changing from 90.2% at $x = 0.15$ to 109.8% at $x = 0.25$. The enhancement $\Delta E_{\text{MAE}}/E_{\text{MAE}}(x = 0.15)$ is about 22%, in striking agreement with the experimental result.

For comparison, in Fig. 4(b) we plot the doping dependence of experimentally extracted MAE, which includes both the ferroelectric-polarization-doping results and those of chemical doping obtained from single-layer samples (a 4 nm LSMO with $x = 0.2$ and a 6 nm LSMO with $x = 0.33$). The general trend of the experimental results is consistent with our theoretical modeling, indicating that the MAE increases with increasing doping level, independent of whether this doping is induced via electrostatic or chemical means. On the other hand, while the MAE for the $x = 0.2$ sample is fully in line with those for the polarization doping results, E_{MAE} for the $x = 0.33$ single-layer sample is only 17% higher than that of the $x = 0.2$ sample, considerably lower than the theoretically projected value of 26% for this doping change. Such discrepancy can be understood by taking epitaxial strain into account. To mimic the field effect condition, the DFT calculations were performed on the bulk $La_{0.8}Sr_{0.2}MnO_3$ structure at a fixed strain level. In contrast, the lattice parameter for bulk LSMO varies for different compositions. The $x = 0.33$ sample is subjected to a larger tensile strain on STO [28], which suppresses the in-plane MAE, as shown both experimentally [49] and theoretically (Supplemental Material [25]).

In previous experimental studies, the doping dependence of MAE has been attributed to the change in d-orbital occupancy [22,42,50]. We employed second-order perturbation theory to model the orbital effect on MAE. The MAE is determined by the matrix elements of the SOC Hamiltonian $H_{\text{SOC}} = \xi \mathbf{L}\cdot\mathbf{S}$ between the occupied and unoccupied states, with ξ being the SOC constant. As the exchange splitting between the majority- and minority-spin bands is sufficiently large in LSMO, we assume for simplicity that only transitions between the majority-spin states play a role. In this case, the MAE can be written as follows [51]:

$$E_{\text{MAE}} = \sum_{n,n'} \frac{|\langle\psi_{n'}|H_{\text{SOC}}|\psi_n\rangle|^2}{\varepsilon_n - \varepsilon_{n'}}, \tag{2}$$

where $\psi_n(\psi_{n'})$ and $\varepsilon_n(\varepsilon_{n'})$ are the majority-spin wave functions and energies of occupied (unoccupied) states, respectively. The matrix elements of H_{SOC} between different d orbitals (d_{xy}, d_{yz}, d_{xz}, d_{z^2}, $d_{x^2-y^2}$) within the orthorhombic coordinates are given in the Supplemental Material [25]. Note that in the conventional cubic coordinate system, the x' and y' axes are aligned along the Mn-O bonding direction, and the $d_{x'z'}$ and $d_{y'z'}$ states are degenerate due to the twofold rotational symmetry about the x axis, which makes a 45° angle with x' [Fig. 4(c)]. This degeneracy, however, is lifted in the orthorhombic structure with the MnO_6 octahedral tilting along $[100]_o$, which yields a uniaxial magnetic anisotropy [31]. To calculate the energy splitting between the d_{xz} and d_{yz} orbitals,

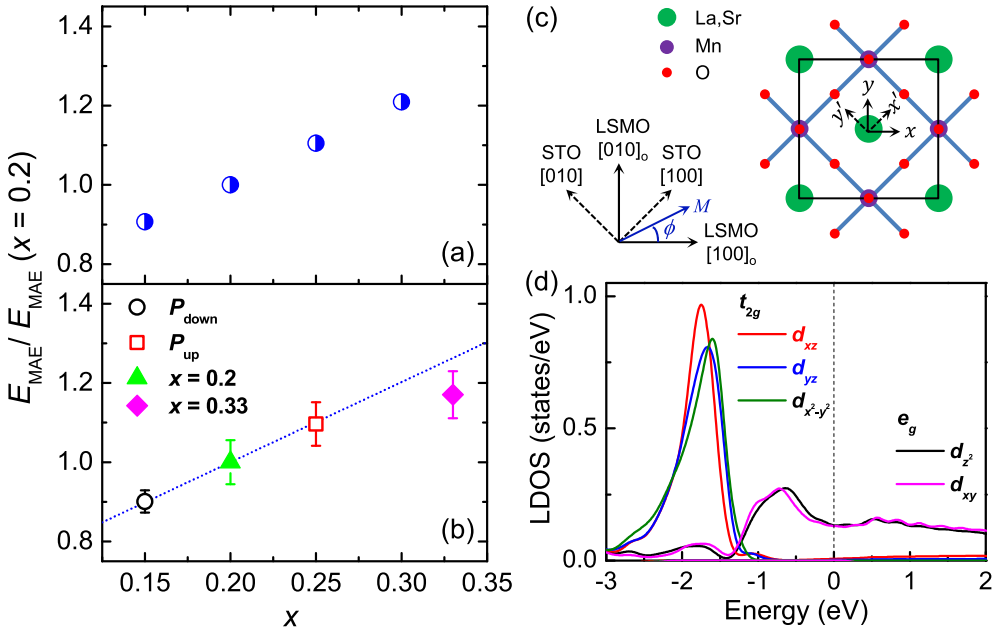

FIG. 4. (a) DFT calculations of normalized MAE as a function of hole doping x and (b) experimental values extracted from the PZT/4 nm LSMO heterostructure in the P_{down} (open circle) and P_{up} (open square) states, a 4 nm LSMO film with $x = 0.2$ (solid triangle), and a 6 nm LSMO film with $x = 0.33$ (solid diamond). The dotted line is projected based on the theoretical results in (a). (c) Top view of LSMO crystal structure. The $x - y$ coordinate system is rotated by 45° with respect to $x' - y'$. (d) LDOS projected onto the Mn-3d orbitals for bulk $La_{0.8}Sr_{0.2}MnO_3$ in the orthorhombic structure, with the d_{xy} and $d_{x^2-y^2}$ orbitals interchanged. The Fermi level lies at zero energy.

we rotated the coordinate system by 45° and calculated the local density of states (LDOS) in the x-y coordinate system. After rotation, the d_{xy} and $d_{x^2-y^2}$ orbitals are interchanged compared with those in the cubic coordinates.

Figure 4(d) shows the calculated orbital-resolved LDOS of bulk LSMO. In LSMO, the majority-spin t_{2g} orbitals are fully occupied and form relatively narrow bands, while the majority-spin e_g orbitals are partly occupied and form relatively broad bands. As expected, the d_{xz} and d_{yz} orbitals are now split, with the d_{xz} orbital LDOS lying at lower energy. In Eq. (2), the only matrix elements of SOC that need to be considered when evaluating the MAE are those between the occupied (d_{yz}, d_{xz}) and unoccupied (d_{xy},d_{z^2}) orbitals (Eq. (S1) in Supplemental Material [25]). To further simplify the description, we assumed that the occupied d_{yz} and d_{xz} orbitals are located at fixed energies ε_{yz} and ε_{xz}, respectively, and the d_{xy} and d_{z^2} bands formed from the e_g orbitals have the same DOS $\rho(\varepsilon)$. In this case, the MAE can be written as follows:

$$E_{MAE} = \xi^2(K + 3K')\sin^2\phi + \xi^2(K' + 3K)\cos^2\phi, \qquad (3)$$

where ϕ is the azimuthal angle [Fig. 4(c)], $K \equiv \int_{E_F}^{+\infty} \frac{\rho(\varepsilon)}{\varepsilon_{yz}-\varepsilon} d\varepsilon$, $K' \equiv \int_{E_F}^{+\infty} \frac{\rho(\varepsilon)}{\varepsilon_{xz}-\varepsilon} d\varepsilon$, and E_F is the Fermi energy. Eliminating the terms independent of ϕ, Eq. (3) can be rewritten as

$$E_{MAE} = 2\xi^2(K' - K)\sin^2\phi. \qquad (4)$$

As the d_{xz} band lies at lower energy than the d_{yz} band, $\varepsilon_{yz} - \varepsilon_{xz} > 0$ and therefore $K' - K > 0$. This implies that E_{MAE} reaches the lowest value at $\phi = 0°$, and thus the $[100]_o$ direction of LSMO is the easy axis.

In this scenario, the doping dependence of the MAE originates from the shift of the Fermi energy. With increasing hole concentration, E_F moves down, which enhances $K' - K$ and hence the MAE. Due to the weak energy dependence of $\rho(\varepsilon)$ around E_F, the variation in MAE $\Delta E_{MAE} \equiv E_{MAE}(x) - E_{MAE}(x_0)$ can be written as follows:

$$\Delta E_{MAE} \approx 2\xi^2(x - x_0)\frac{\varepsilon_{yz} - \varepsilon_{xz}}{(\varepsilon_{xz} - E_F)(\varepsilon_{yz} - E_F)}\sin^2\phi, \qquad (5)$$

where x_0 is the reference doping level. Our simple model based on second-order perturbation theory thus predicts a $\sin^2\phi$ dependence of the MAE, with ΔE_{MAE} scaling linearly with the doping level x, which is consistent with the experimental results and the explicit DFT calculations (Figs. 4(a), 4(b), and Supplemental Material [25]). This decisive role of the d-orbital population in voltage-controlled magnetic anisotropy has also been predicted in transition-metal-based magnetic tunnel junctions [51].

In summary, exploiting the planar Hall technique, we have quantitatively assessed the ferroelectric polarization control of the in-plane magnetic anisotropy in LSMO thin films, which allows us to unambiguously separate the effects of charge doping and lattice distortion to the MCA. Our DFT calculations combined with second-order perturbation theory show that the anisotropy energy increases linearly with hole doping, agreeing well with the experimental observations and pointing to the critical role of the d-orbital population in controlling the MCA. Our work provides insights into the effect of electrostatic doping on magnetic anisotropy in strongly correlated magnetic oxide materials, which can facilitate the development of high-performance, low-power spintronic devices.

We would like to thank Xuegang Chen and Balasubramanian Balamurugan for technical assistance. This work

was supported by the National Science Foundation (NSF) through the Nebraska Materials Research Science and Engineering Center (MRSEC) Grant No. DMR-1420645 (sample preparation and theoretical modeling) and NSF CAREER Grant No. DMR-1148783 (studies of PZT/LSMO heterostructures). Work by Y.H. was supported by NSF Grant No. DMR-1710461 (studies of LSMO thin films). Work by J.S. was supported by the U.S. Department of Energy (DOE), Office of Science, Basic Energy Sciences (BES) under Award No. DE-SC0016153 (PFM characterization). The research was performed in part at the Nebraska Nanoscale Facility: National Nanotechnology Coordinated Infrastructure and the Nebraska Center for Materials and Nanoscience, which are supported by the NSF under Award ECCS: 1542182, and the Nebraska Research Initiative. Computations were performed at the University of Nebraska Holland Computing Center.

[1] J. P. Velev, S. S. Jaswal, and E. Y. Tsymbal, Multiferroic and magnetoelectric materials and interfaces, Philos. Trans. R. Soc. A Math. Phys. Engineer. Sci. **369**, 3069 (2011).

[2] C. A. F. Vaz and U. Staub, Artificial multiferroic heterostructures, J. Mater. Chem. C **1**, 6731 (2013).

[3] F. Matsukura, Y. Tokura, and H. Ohno, Control of magnetism by electric fields, Nat. Nanotechnol. **10**, 209 (2015).

[4] X. Hong, Emerging ferroelectric transistors with nanoscale channel materials: The possibilities, the limitations, J. Phys. Condens. Matter **28**, 103003 (2016).

[5] E. Y. Tsymbal, A. Gruverman, V. Garcia, M. Bibes, and A. Barthelemy, Ferroelectric and multiferroic tunnel junctions, MRS Bull. **37**, 138 (2012).

[6] S. Fusil, V. Garcia, A. Barthelemy, and M. Bibes, Magnetoelectric devices for spintronics, Annu. Rev. Mater. Res. **44**, 91 (2014).

[7] C. G. Duan, J. P. Velev, R. F. Sabirianov, Z. Q. Zhu, J. H. Chu, S. S. Jaswal, and E. Y. Tsymbal, Surface Magnetoelectric Effect in Ferromagnetic Metal Films, Phys. Rev. Lett. **101**, 137201 (2008).

[8] T. Maruyama, Y. Shiota, T. Nozaki, K. Ohta, N. Toda, M. Mizuguchi, A. A. Tulapurkar, T. Shinjo, M. Shiraishi, S. Mizukami, Y. Ando, and Y. Suzuki, Large voltage-induced magnetic anisotropy change in a few atomic layers of iron, Nat. Nanotechnol. **4**, 158 (2009).

[9] W.-G. Wang, M. Li, S. Hageman, and C. L. Chien, Electric-field-assisted switching in magnetic tunnel junctions, Nat. Mater. **11**, 64 (2012).

[10] Y. Shiota, T. Nozaki, F. Bonell, S. Murakami, T. Shinjo, and Y. Suzuki, Induction of coherent magnetization switching in a few atomic layers of FeCo using voltage pulses, Nat. Mater. **11**, 39 (2012).

[11] P. V. Lukashev, J. D. Burton, S. S. Jaswal, and E. Y. Tsymbal, Ferroelectric control of the magnetocrystalline anisotropy of the Fe/$BaTiO_3$(001) interface, J. Phys.: Condens. Matter **24**, 226003 (2012).

[12] J.-M. Hu, C.-W. Nan, and L.-Q. Chen, Size-dependent electric voltage controlled magnetic anisotropy in multiferroic heterostructures: Interface-charge and strain comediated magnetoelectric coupling, Phys. Rev. B **83**, 134408 (2011).

[13] C.-G. Duan, J. P. Velev, R. F. Sabirianov, W. N. Mei, S. S. Jaswal, and E. Y. Tsymbal, Tailoring magnetic anisotropy at the ferromagnetic/ferroelectric interface, Appl. Phys. Lett. **92**, 122905 (2008).

[14] X. Hong, A. Posadas, A. Lin, and C. H. Ahn, Ferroelectric-field-induced tuning of magnetism in the colossal magnetoresistive oxide $La_{1-x}Sr_xMnO_3$, Phys. Rev. B **68**, 134415 (2003).

[15] X. Hong, J. B. Yau, J. D. Hoffman, C. H. Ahn, Y. Bason, and L. Klein, Effect of electric field doping on the anisotropic magnetoresistance in doped manganites, Phys. Rev. B **74**, 174406 (2006).

[16] H. J. A. Molegraaf, J. Hoffman, C. A. F. Vaz, S. Gariglio, D. van der Marel, C. H. Ahn, and J.-M. Triscone, Magnetoelectric effects in complex oxides with competing ground states, Adv. Mater. **21**, 3470 (2009).

[17] C. A. F. Vaz, J. Hoffman, Y. Segal, J. W. Reiner, R. D. Grober, Z. Zhang, C. H. Ahn, and F. J. Walker, Origin of the Magnetoelectric Coupling Effect in $Pb(Zr_{0.2}Ti_{0.8})O_3/La_{0.8}Sr_{0.2}MnO_3$ Multiferroic Heterostructures, Phys. Rev. Lett. **104**, 127202 (2010).

[18] S. M. Wu, S. A. Cybart, P. Yu, M. D. Rossell, J. X. Zhang, R. Ramesh, and R. C. Dynes, Reversible electric control of exchange bias in a multiferroic field-effect device, Nat. Mater. **9**, 756 (2010).

[19] H. Lu, T. A. George, Y. Wang, I. Ketsman, J. D. Burton, C. W. Bark, S. Ryu, D. J. Kim, J. Wang, C. Binek, P. A. Dowben, A. Sokolov, C. B. Eom, E. Y. Tsymbal, and A. Gruverman, Electric modulation of magnetization at the $BaTiO_3/La_{0.67}Sr_{0.33}MnO_3$ interfaces, Appl. Phys. Lett. **100**, 232904 (2012).

[20] S. M. Wu, S. A. Cybart, D. Yi, J. M. Parker, R. Ramesh, and R. C. Dynes, Full Electric Control of Exchange Bias, Phys. Rev. Lett. **110**, 067202 (2013).

[21] D. Yi, J. Liu, S. Okamoto, S. Jagannatha, Y. C. Chen, P. Yu, Y. H. Chu, E. Arenholz, and R. Ramesh, Tuning the Competition Between Ferromagnetism and Antiferromagnetism in a Half-Doped Manganite through Magnetoelectric Coupling, Phys. Rev. Lett. **111**, 127601 (2013).

[22] D. Preziosi, I. Fina, E. Pippel, D. Hesse, X. Marti, F. Bern, M. Ziese, and M. Alexe, Tailoring the interfacial magnetic anisotropy in multiferroic field-effect devices, Phys. Rev. B **90**, 125155 (2014).

[23] T. L. Meyer, A. Herklotz, V. Lauter, J. W. Freeland, J. Nichols, E. J. Guo, S. Lee, T. Z. Ward, N. Balke, S. V. Kalinin, M. R. Fitzsimmons, and H. N. Lee, Enhancing interfacial magnetization with a ferroelectric, Phys. Rev. B **94**, 174432 (2016).

[24] S. Zhang, Y. G. Zhao, X. Xiao, Y. Z. Wu, S. Rizwan, L. F. Yang, P. S. Li, J. W. Wang, M. H. Zhu, H. Y. Zhang, X. F. Jin, and X. F. Han, Giant electrical modulation of magnetization in $Co_{40}Fe_{40}B_{20}/Pb(Mg_{1/3}Nb_{2/3})_{0.7}Ti_{0.3}O_3$(011) heterostructure, Sci. Rep. **4**, 3727 (2014).

[25] See Supplemental Material at http://link.aps.org/supplemental/10.1103/PhysRevMaterials.3.021401 for details of sample growth and characterization, PHE studies of single-layer LSMO, and DFT calculations.

[26] X. G. Chen, X. Zhang, M. A. Koten, H. H. Chen, Z. Y. Xiao, L. Zhang, J. E. Shield, P. A. Dowben, and X. Hong, Interfacial charge engineering in ferroelectric-controlled Mott transistors, Adv. Mater. **29**, 1701385 (2017).

[27] L. C. Tanase, L. E. Abramiuc, D. G. Popescu, A. M. Trandafir, N. G. Apostol, I. C. Bucur, L. Hrib, L. Pintilie, I. Pasuk, L. Trupina, and C. M. Teodorescu, Polarization Orientation in Lead Zirconate Titanate (001) Thin Films Driven by the Interface with the Substrate, Phys. Rev. Appl. **10**, 034020 (2018).

[28] A. Urushibara, Y. Moritomo, T. Arima, A. Asamitsu, G. Kido, and Y. Tokura, Insulator-metal transition and giant magnetoresistance in $La_{1-x}Sr_xMnO_3$, Phys. Rev. B **51**, 14103 (1995).

[29] X. Hong, A. Posadas, and C. H. Ahn, Examining the screening limit of field effect devices via the metal-insulator transition, Appl. Phys. Lett. **86**, 142501 (2005).

[30] M. Huijben, L. W. Martin, Y. H. Chu, M. B. Holcomb, P. Yu, G. Rijnders, D. H. A. Blank, and R. Ramesh, Critical thickness and orbital ordering in ultrathin $La_{0.7}Sr_{0.3}MnO_3$ films, Phys. Rev. B **78**, 094413 (2008).

[31] A. Rajapitamahuni, L. Zhang, M. A. Koten, V. R. Singh, J. D. Burton, E. Y. Tsymbal, J. E. Shield, and X. Hong, Giant Enhancement of Magnetic Anisotropy in Ultrathin Manganite Films via Nanoscale 1D Periodic Depth Modulation, Phys. Rev. Lett. **116**, 187201 (2016).

[32] L. Zhang, A. Rajapitamahuni, Y. Hao, and X. Hong, Probing magnetic anisotropy in epitaxial $La_{0.67}Sr_{0.33}MnO_3$ thin films and nanostructures via planar Hall effect, Proc. SPIE **10732**, 107320F (2018).

[33] J. B. Yau, X. Hong, A. Posadas, C. H. Ahn, W. Gao, E. Altman, Y. Bason, L. Klein, M. Sidorov, and Z. Krivokapic, Anisotropic magnetoresistance in colossal magnetoresistive $La_{1-x}Sr_xMnO_3$ thin films, J. Appl. Phys. **102**, 103901 (2007).

[34] Y. Bason, L. Klein, J. B. Yau, X. Hong, and C. H. Ahn, Giant planar Hall effect in colossal magnetoresistive $La_{0.84}Sr_{0.16}MnO_3$ thin films, Appl. Phys. Lett. **84**, 2593 (2004).

[35] K. Steenbeck and R. Hiergeist, Magnetic anisotropy of ferromagnetic $La_{0.7}(Sr,Ca)_{0.3}MnO_3$ epitaxial films, Appl. Phys. Lett. **75**, 1778 (1999).

[36] N. Naftalis, Y. Bason, J. Hoffman, X. Hong, C. H. Ahn, and L. Klein, Anisotropic magnetoresistance and planar Hall effect in epitaxial films of $La_{0.7}Ca_{0.3}MnO_3$, J. Appl. Phys. **106**, 023916 (2009).

[37] H. X. Tang, R. K. Kawakami, D. D. Awschalom, and M. L. Roukes, Giant Planar Hall Effect in Epitaxial (Ga,Mn)As Devices, Phys. Rev. Lett. **90**, 107201 (2003).

[38] Y. Bason, L. Klein, H. Q. Wang, J. Hoffman, X. Hong, V. E. Henrich, and C. H. Ahn, Planar Hall effect in epitaxial thin films of magnetite, J. Appl. Phys. **101**, 09J507 (2007).

[39] J. D. Hoffman, S. M. Wu, B. J. Kirby, and A. Bhattacharya, Tunable Noncollinear Antiferromagnetic Resistive Memory through Oxide Superlattice Design, Phys. Rev. Appl. **9**, 044041 (2018).

[40] Y. Bason, L. Klein, J. B. Yau, X. Hong, J. Hoffman, and C. H. Ahn, Planar Hall-effect magnetic random access memory, J. Appl. Phys. **99**, 08R701 (2006).

[41] C. Tannous and J. Gieraltowski, The Stoner–Wohlfarth model of ferromagnetism, Eur. J. Phys. **29**, 475 (2008).

[42] B. Cui, C. Song, G. A. Gehring, F. Li, G. Y. Wang, C. Chen, J. J. Peng, H. J. Mao, F. Zeng, and F. Pan, Electrical manipulation of orbital occupancy and magnetic anisotropy in manganites, Adv. Func. Mater. **25**, 864 (2015).

[43] D. Vanderbilt, Soft self-consistent pseudopotentials in a generalized eigenvalue formalism, Phys. Rev. B **41**, 7892(R) (1990).

[44] P. Giannozzi, S. Baroni, N. Bonini, M. Calandra, R. Car, C. Cavazzoni, D. Ceresoli, G. L. Chiarotti, M. Cococcioni, I. Dabo, A. D. Corso, S. d. Gironcoli, S. Fabris, G. Fratesi, R. Gebauer, U. Gerstmann, C. Gougoussis, A. Kokalj, M. Lazzeri, L. Martin-Samos, N. Marzari, F. Mauri, R. Mazzarello, S. Paolini, A. Pasquarello, L. Paulatto, C. Sbraccia, S. Scandolo, G. Sclauzero, A. P. Seitsonen, A. Smogunov, P. Umari, and R. M. Wentzcovitch, QUANTUM ESPRESSO: A modular and open-source software project for quantum simulations of materials, J. Phys. Condens. Matter **21**, 395502 (2009).

[45] J. P. Perdew, K. Burke, and M. Ernzerhof, Generalized Gradient Approximation Made Simple, Phys. Rev. Lett. **77**, 3865 (1996).

[46] J. D. Burton and E. Y. Tsymbal, Prediction of electrically induced magnetic reconstruction at the manganite/ferroelectric interface, Phys. Rev. B **80**, 174406 (2009).

[47] J. D. Burton and E. Y. Tsymbal, Giant Tunneling Electroresistance Effect Driven by an Electrically Controlled Spin Valve at a Complex Oxide Interface, Phys. Rev. Lett. **106**, 157203 (2011).

[48] F. Sandiumenge, J. Santiso, L. Balcells, Z. Konstantinovic, J. Roqueta, A. Pomar, J. P. Espinós, and B. Martínez, Competing Misfit Relaxation Mechanisms in Epitaxial Correlated Oxides, Phys. Rev. Lett. **110**, 107206 (2013).

[49] G. Panchal, D. M. Phase, V. R. Reddy, and R. J. Choudhary, Strain-induced elastically controlled magnetic anisotropy switching in epitaxial $La_{0.7}Sr_{0.3}MnO_3$ thin films on $BaTiO_3(001)$, Phys. Rev. B **98**, 045417 (2018).

[50] D. Preziosi, M. Alexe, D. Hesse, and M. Salluzzo, Electric-Field Control of the Orbital Occupancy and Magnetic Moment of a Transition-Metal Oxide, Phys. Rev. Lett. **115**, 157401 (2015).

[51] J. Zhang, P. V. Lukashev, S. S. Jaswal, and E. Y. Tsymbal, Model of orbital populations for voltage-controlled magnetic anisotropy in transition-metal thin films, Phys. Rev. B **96**, 014435 (2017).